PAPER

Characterization and nonlinear models of bending extensile/contractile pneumatic artificial muscles

View the article online for updates and enhancements.

Characterization and nonlinear models of bending extensile/contractile pneumatic artificial muscles

Qinghua Guan[1] , Jian Sun[1], Yanju Liu[2] , Norman M Wereley[3] and Jinsong Leng[1]

[1] Centre for Composite Materials and Structures, Science Park of Harbin, Institute of Technology (HIT), Harbin, People's Republic of China
[2] Department of Astronautical Science and Mechanics, Harbin Institute of Technology (HIT), Harbin, People's Republic of China
[3] Department of Aerospace Engineering, University of Maryland, College Park, MD 20742, United States of America

E-mail: lengjs@hit.edu.cn

Abstract

Pneumatic artificial muscles (PAMs) are compliant fluidic actuators, usually consisting of a tubular bladder, a braided sleeve and end fittings. PAMs have been studied extensively by researchers; however, most previous researches are focused on the axial PAMs. Herein, a pair of nonlinear models were developed based on the principle of virtual work and the force balance analysis. And the two models are applicable to both bending extensile PAMs (BE-PAMs) and bending contractile PAMs (BC-PAMs). In this study, a cyclic bending moment loading experimental method were proposed and conducted with BE-PAMs and BC-PAMs to characterize their deformation and actuation performance and draw their overall relationships of actuation moment to bending curvature and inner pressure. With the experimental results, the validation analysis was carried out to demonstrate the validity of the two models. The energy model can get higher accuracy, while the force balance model could provide more details of the interior and interaction stress conditions. The combination of both can promote the comprehension of non-axial bending PAMs. Moreover, two three-finger soft grippers and a humanoid hand based on BE-PAMs and BC-PAMs were built and tested to investigate their performance on gripping objects. The BE-PAM gripper showed more accommodative gripping performance, whereas, the BC-PAM gripper owned higher gripping force. The humanoid hand combining the merits of both showed excellent flexibility, adaptability and decent load capability in gripping object with various sizes, shapes and materials.

Keywords: bending actuator, soft robotics, extensile, pneumatic, self-sensing

(Some figures may appear in colour only in the online journal)

1. Introduction

Pneumatic artificial muscles (PAMs) are compliant fluidic actuators, usually consisting of a tubular bladder, a braided sleeve and end fittings, among which the earliest and most well-known one is McKibben actuator. With the thriving of soft robotics, as one of earliest researched soft actuators, PAMs have gained increasing attention from the general field of robotics again.

Axial contractile PAMs have been widely applied to bio-robotics, humanoid robots, rehabilitation devices, which were collected by Georgios Andrikopoulos *et al* [1]. But due to its much higher stiffness after inflation, the axial contractile PAMs are hard to bend and show less flexibility, especially for wearable devices and soft robots. As a result, the axial contractile PAMs were usually utilized as pneumatic cylinders instead of soft joints. Meanwhile, the extensile PAM have increasingly attracted researchers' eyes owing to its excellent

deformability and compliance [2–5], even though it was long neglected due to low output force and tendency to buckle under external loads [4]. Recently, some new types of PAM have been developed and applied to soft robotics by researches including bending extensile PAMs (BE-PAMs) [6–8]/bending contractile PAMs (BC-PAMs), helical extensile/contractile PAMs [9] and Variable Stiffness Extensor-Contractor [10], which promotes the blossom of PAMs. It is worth noting that the BC-PAMs improved the flexibility of axial contractile PAMs significantly, which enables contractile PAMs could be more widely applied to soft robotics.

In soft robotics, the bending actuator is always the central topic, since it provides the most essential motion, and can be utilized in most of soft robots. Moreover, the researches of bending actuators can be further wielded as the foundation of other more complicated actuators such as helical and multi-degree-of-freedom (DOF) actuators. However, predicting the performance of soft actuators is nontrivial due to their nonlinear response and complex geometry [11].

Various static and dynamic models have been built for PAMs to accurately predict their performance and are based on virtual work theorem [12–14], force balance analysis [15], hyperelastic nonlinear analysis [16, 17], numerical or finite element analysis [18, 19] and a variety of modifications. Zhiye Zhang *et al* and Bertrand Tondu have done excellent summary of these modeling methods [20, 21]. However, these studies were focused on axial PAMs (either contractile or extensile), and there are limited models available for soft BE-PAMs or BC-PAMs [7–9, 22], thus constraining their possibilities as an attractive class of soft actuators [11]. Hassanin Al-Fahaam *et al* built an output force mathematical model for extensor bending PAMs considering the non-constant braid angle around the circumference by introducing a circular cross-section of the nominal radius derived from the braid angles of the innermost and outermost points of the bending actuator surface, with assumptions that there are not elastic forces within the rubber [7, 8].

In addition, to investigate the performance of soft bending actuators, the interaction force or torque were usually chosen in the output test considering the testing convenience and consistency with application conditions. And there have been amounts of methods proposed to test the interaction force. Pressure sensor [11, 23], torque sensor [24] and multi-axis force/torque [11, 25–27] sensors were fixed or mounted on an orbit [24] to conduct the isometric test or isotonic test. However, different contact and constraint conditions result in discrepant boundary conditions in mechanics. As a consequence, the interaction force measured experimentally will vary with different testing methods, which makes it difficult to comparatively analyze these test results from diverse actuator test methods. Additionally, different interaction forces can generate various non-uniform distribution of bending loads and bring non-constant curvature configuration, which is rarely considered in the validations of prior studies and undermines the consistency between theories and experiments. Moreover, unlike the rigid hinge with limited DOF, for soft bending actuators with infinite DOF in theory, the trajectory of the tip end is complex and non-unique. As a result, the cyclic loading test of interaction force at the tip is usually hard to be applied to the bending actuator. While the hysteresis in the cyclic loading is the primary evaluative criteria for the damping property which is non-negligible for some soft actuators, especially for PAMs.

In this study, BE-PAM and BC-PAM were built with homologous structures by reinforced along the axis with an elastic frame with enough stiffness to restrain extension or contraction and resist buckling, which offers a chance to characterize and compare the performances of BE-PAMs and BC-PAMs with a homotypic structural design. Moreover, in this study, a four-point moment cyclic loading test method was proposed to facilitate the assessment and comparison of bending actuators. With this method, uniform bending loads could be applied during the cyclic test. And it would bring more consistency between experimental results and theoretical analyses and make it more convenient to estimate the energy losses of bending actuator.

To solving the error brought by the neglect of elastic forces, in models of this study, based on our prior works [9], not only the non-constant braid angle and the effect of elastic deformation of the rubber tube and elastic frame were considered, but also the nonlinear behavior of bladder tube materials was also involved with the Mooney–Rivlin hyperelastic model.

Finally, two three-finger grippers and a humanoid hand with multi-direction bending wrist based on BE-PAMs and BC-PAMs were developed to demonstrate their performance on robotics, in which the BE-PAM gripper showed more accommodative gripping performance due to its better compliance, larger strokes and flexibility. Whereas, the BC-PAM gripper owned higher gripping force. Based on their characterization and performance, a humanoid hand with fingers, palm and wrist was built. The fingers and palm were actuated by BE-PAM showed excellent flexibility and adaptability in gripping object with various sizes, shapes and materials. And the wrist built with BC-PAM achieved four direction bending and exhibited decent load capability.

2. Bending extensile and contractile PAMs

BE-PAM and BC-PAM are consists of end fittings, an elastic tube, a braided tube and an embedded elastic frame (figure 1). The braid angle α (figure 2(b)) of axial contractile PAM usually should be lower than the critical angle of 54.74°, at which the PAM has the maximum volume. As a result, when inflated the braid angle of contractile PAM increases and the PAM contracts (figure 1(b)). Based on the same principles, the axial extensile PAM could be realized by adjusting the braid angle above 54.74° (figure 1(a)). In this work, to achieve the bending motion, an elastic frame is placed concentrically between the bladder and braided tubes (figures 1(c) and (d)) to constrain the contraction/extension deformation on one side and generate a bending deformation toward or against the reinforced side when inflated, as shown in figures 1(c)–(f). Moreover, as the frame is flexible and relatively un-stretchable, it could be utilized as a substrate for a flexible sensor.
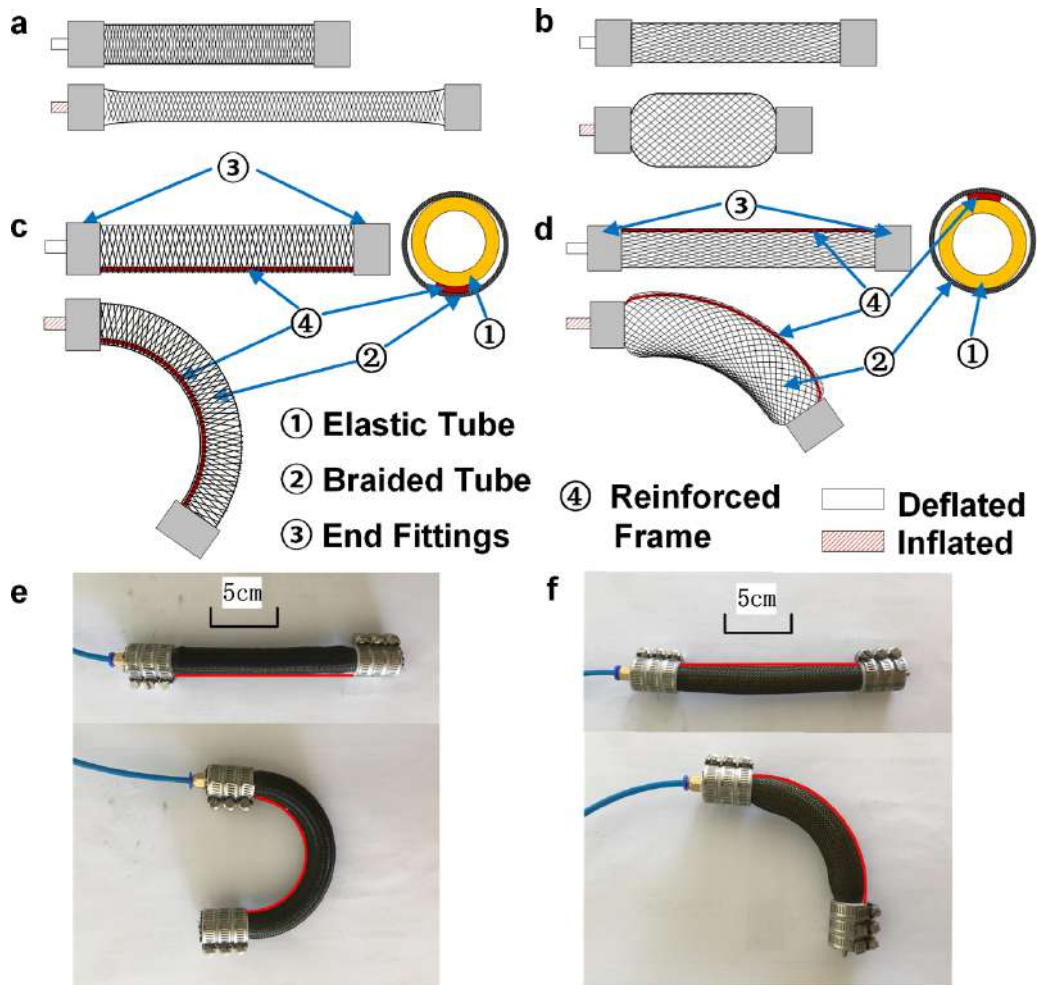
Figure 1. Schematic diagrams of conventional extensile and contractile PAMs (a), (b) and bending extensile and contractile PAMs (c), (d): (e) and (f) show the simples of bending extensile PAM (BE-PAM) and bending contractile PAM (BC-PAM). The red curve is the position of reinforced elastic frame to restrict the extension or contraction of one side and generate the bending deformation in the corresponding direction.
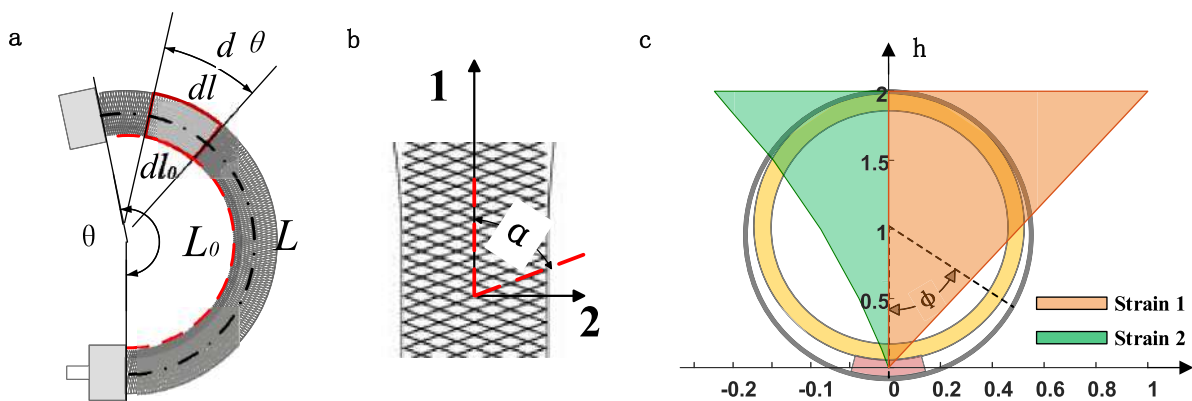

Figure 2. Kinematics of bending PAM: (a) main parameters of the BE-PAM are the bending angle θ, the initial active length L_0 and the deformed axial length L; (b) the definition of braid angle α: direction 1 is the axial direction, and direction 2 is the circular direction; (c) the inhomogeneous strain distributions at a typical cross-section, of which the initial braid angle $\alpha_0 = 75°$ and the axial elongation ratio $\lambda_{axis} = 1.5$. ϕ is the cylindrical coordinate defined in the plane of the cross section.

2.1. Kinematic parameters of bending PAMs

Unlike the axial PAMs, the deformation distribution of bending PAMs at the cross section is uneven. The mechanism distinction between bending and axial PAMs generates the need to analyze bending PAMs in an unusual way. Guan *et al* developed a kinematic model to describe the general bending behaviors of PAMs including BE-PAMs and BC-PAMs [9].

Figure 2 shows the kinematic parameters of bending PAMs. α is the braid angle. λ_1 and λ_2 are stretch ratios of the braid along the axial and circular directions (figure 2(b)). L_0 is the length of the inextensible and uncompressible frame and the initial axis, and L is the deformed axis length of (figure 2(a)). θ is the bending angle of the actuator, and k is the bending curvature of the actuator axis (figure 2(a)). Moreover, the bending curvature of the elastic frame k' was introduced to simplify the analysis as equation (1).

$$k = 1/\left(\frac{1}{k'} + R\right) = k'/\left(1 + k'R\right). \tag{1}$$

Due to the constraints of the braid, the relation of axial strain, ε_1 and circular strain ε_2 can be written as below,

$$[\cos\alpha_0\left(1 + \varepsilon_1\right)]^2 + [\sin\alpha_0\left(1 + \varepsilon_2\right)]^2$$
$$= \cos^2\alpha_0\lambda_1{}^2 + \sin^2\alpha_0\lambda_2{}^2 = 1. \tag{2}$$

Then ε_1 and ε_2 can be written as a function of k' and the distance to the frame h or the cylindrical coordinate Φ at the cross section as equation (3), shown in figure 2(c). And the braid angle around the circumstance can also be obtained from the equation (4),

$$\varepsilon_1 = \lambda_1 - 1 \approx k'h = k'\left(1 - \cos\Phi\right)R \tag{3}$$

$$\varepsilon_2 = \frac{\sqrt{1 - [\cos\alpha_0\left(1 + \varepsilon_1\right)]^2}}{\sin\alpha_0} - 1 = \frac{\sin\alpha\left(\Phi\right)}{\sin\alpha_0} - 1 = \lambda_2 - 1. \tag{4}$$

Here, it is defined that the bending curvature k' is positive when the actuator longitudinal axis bends towards to the reinforced side, otherwise it is negative. Here, it is assumed that after inflation and bending, the actuator still maintains its circular cross section to simplify the analysis, even though the circular cross section of inflated actuator is not a perfect circle. And the length of the elastic frame is also assumed as a constant. Then relationship between the radius and bending curvature of elastic frame can be defined as below [9].

$$\eta_1 = \frac{R}{R_0} = \frac{2\pi}{\sin\alpha_0} \times \frac{1}{\int_0^{2\pi} \frac{1}{\sqrt{1 - [\cos\alpha_0 1 + k'R(1 - \cos\Phi)]^2}}\mathrm{d}\Phi}$$
$$= \xi\left(k'R, \alpha_0\right) = \eta\left(k', \alpha_0\right). \tag{5}$$

2.2. Cyclic moment loading test

To comprehensively characterize the mechanical properties of BE-PAM/BC-PAM and understand especially the effect of the elastic bladder and flexible frame, a BE-PAM and a BC-PAM were built for quasi-static tests with braid angle of 68.0° and 35.0° (figure 3(a)). The BE-PAM and BC-PAM were both built with polyethylene terephthalate braided sleeve tube, latex

Table 1. Geometry and material property parameters of BE-PAM and BC-PAM for cyclic tests.

	BE-PAM	BC-PAM
The original braid angle α_0	68.0°	35°
The original length L_0	145 mm	
Outer radius R_0 of the bladder tube	8.5 mm	
Thickness t_0 of the bladder tube	2.5 mm	
Dimensions of the flexible frame	0.5 mm (thickness) × 5 mm (width)	
Elastic modulus of the flexible frame	6.796 GPa	
Starting threshold pressure P_{start}	0.068 MPa	
Starting actuator radius $R_{0,\,\text{start}}$	10.1 mm	8.6 mm

bladder tube, glass fiber reinforced epoxy flexible frame, aluminum end fittings and some fasteners. The geometry and material property parameters of the BE-PAM and BC-PAM are summarized in table 1.

The moment load was applied to the actuator via a four-point bending fixture, as shown in figure 3(b). The test was conducted on a Zwick-010 Electro-mechanical Universal Testing Machine under a set of pressures. At each pressure, the actuator was tested with three load cycles starting from the blocked state to the free-bending state and then returning to the blocked state, as shown in figure 3(c). Before the cycle loading test, the position of loading frame at free-bending state was detected via adjusting the position from blocked state till the load reduced to 0.2 N, while the PAM was inflated.

The mechanical parameters and analysis of the Loading device are presented in figure 3(d). F_1, F_2 are loading forces of loading frame 1 and 2. F_{N1}, F_{N2} are the interaction forces applied to each connecting plate by loading frames. d is the horizontal distance between the two loading rollers on the same side. t is the thickness of the connecting plate. $r = 2.5$ mm is the radius of the loading rollers. β is pitch angle of the connecting plate and can be obtained from equation (6). According to the mechanical analysis in figure 3(d) and considering the self-weight effects of the actuator and the connecting plates, the applied moment and bending curvature can be calculated as follows.

$$d \cdot \tan\beta + \left(\sqrt{1 + \tan^2\beta} - 1\right)(t + 2r) = \Delta s \tag{6}$$

$$M = \frac{F_{\text{load}}\left[d + (2r + t)\sin\beta\right]}{2\cos\beta^2}, d = 35\,\text{mm}, r = 2.5\,\text{mm},$$
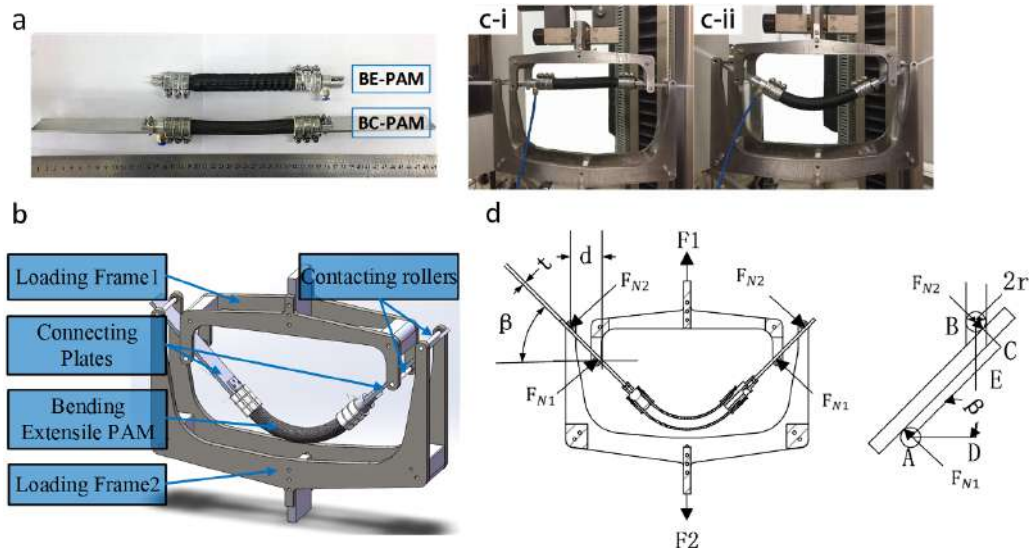$$t = 4\,\text{mm} \tag{7}$$

$$k' = \frac{2\beta}{L_0}. \tag{8}$$

Figure 3. The four point loading fixture for quasi-static moment cyclic loading test: (a) BE-PAM (the initial braid angles $\alpha_0 = 68.0°$) and BC-PAM with mounted connecting plates ($\alpha_0 = 35.0°$); (b) main components of the test fixture; (c) the blocked state (c-i) and the free-bending state (c-ii) of cyclic loading tests; (d) Mechanical parameters and analysis of the Loading device.

F_{load} is the effective applied load of the testing machine that is equal to F_1 in figure 3(b), Δs is the stroke of load frame.

As the original signal of BE-PAM and BC-PAM contained too much noise during the test, there cycle loading curves of each PAM were filtered and averaged to one cycle loading curve to better describe the relationship, as shown in figures 4(a) and (b). For further analysis, the average moments were calculated with the unloading and loading process to eliminate the effect of the hysteresis. It needs to be stated that some deviation occurred to the output moment of the BE-PAM, which was caused by the increasing influence of the actuator self-weight. This was due to the larger bending angle and the descending output actuation moment when close to the free-bending state at pressures of 0.175 MPa and 0.200 MPa. BE-PAM achieved a free-bending curvature of approximately 0.0113 mm^{-1}, and a free-bending angle of 94° under 0.20 MPa. During each cycle (figure 4(c)), the actuator generated the maximum output moment at the blocked state of approximately 300 N mm at 200 kPa (figure 4(d)). Meanwhile, the BC-PAM was tested under the pressure from 40 kPa to 140 kPa (figure 4(b)), and its elastic frame buckled and fractured at the blocked state around the pressure of 200 kPa with the maximum output moment of 802 N mm. At free-bending state, its bending angle is 65° under 200 kPa. The error bars were added in figures 4(c)–(f). The error bars in figures 4(c) and (e) shows the standard errors of block moments in different pressures, which were calculated from the maximum moments of three cycle loading curves. The error bars in figures 4(d) and (f) shows the standard error of free-bending curvatures in different pressures, which were calculated from the data in the free-bending state detection process before the loading test. It needs to be stated that standard error of free-bending curvature for BC-PAM at 140 kPa is much larger than others, which indicated its measurement deviation. And based on the cycle loading curve, the real free-bending curvature (figure 4(b)) may slightly lower than the measured value at 140 kPa, which

could be caused by the increasing bending angle and the larger descending rate of output moment to curvature around the free-bending state. But since the modeling work was based on the whole loading process, the whole loading curve still has reference value for model analysis.

From figures 4(a) and (b), nonlinear behaviors, deadband of pressure and hysteresis effects can be found in the cycling load tests. From the linear fitting line of the experimental results about the block moments (figures 4(c) and (d)), the deadband pressure of BE-PAM and BC-PAM are approximately 68 kPa and 32 kPa, respectively. The energy loss is calculated via the integration of a cyclic loading curve, and the maximum storage energy is obtained by integrating the average loading curve of each cycle. The energy losses ratio is calculated by using the energy loss divided by the maximum storage energy in a loading cycle. The hysteresis effect is more obvious at higher pressures due to the higher interaction forces of the braid fibers and between the braid sleeve and the bladder tube, while the energy losses ratio did not change much due to the concomitant increasing output (figures 4(a) and (b)). It should be noted that at lower pressures close to the threshold pressures, the energy loss ratio is relatively higher, which is caused by the joint effect of low output and indelible residual friction due to the inherent tension of the fabric. The average energy losses ratio of the BE-PAM from 0.1 MPa to 0.2 MPa is approximately 25.57%, and the average losses ratio of the BC-PAM is around 20.89% which is much lower than the former (table 2).

Moreover, from figures 4(d) and (f), the free-bending curvature increased with the working pressure, which indicates that the output actuation moment is also related to the elastic deformation of the bladder and the frame. Thus, the data of moment loads and bending curvatures under a set of pressures can provide a detailed reference for determining the anti-moment generated by the bladder and the frame in the quasi-static model building, discussed in the next section.
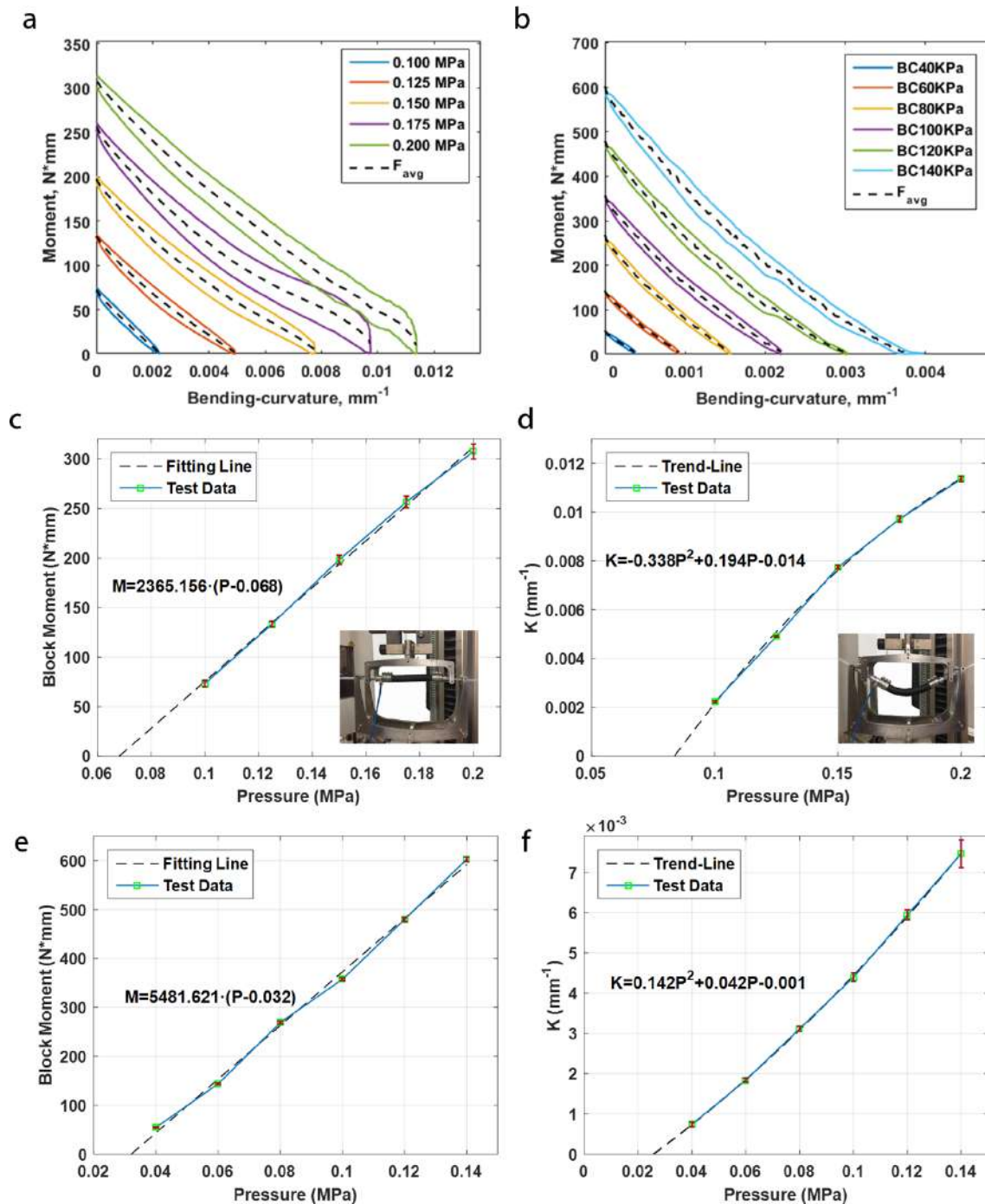
Figure 4. Quasi-static cyclic moment loading test results: Filtered test data of BE-PAM (a) and BC-PAM (b). For each pair of curves is measured at each pressure, the lower curve of each cycle presents the unloading process from blocked state to free bending state and the upper curve of each cycle presents the loading process from free bending state to blocked state. Blocked moment vs. working pressure for BE-PAM (c) and BC-PAM (e), and Free bending curvature vs. working pressure for BE-PAM (d) and BC-PAM (f).

3. Nonlinear quasi-static model development of bending PAMs

For axial PAMs, there are many models describing the relationships among the input air pressure, output force and axial displacement/deformation ratio. In this study, nonlinear quasi-static models were built to describe the relationships among the input air pressure, output moment and bending curvature of the actuator. Two different models based on the principle of virtual work and force balance analysis were developed to predict the mechanical properties and study the working mechanisms. Moreover, the Mooney–Rivlin hyperelastic model (see for example [28]) is applied to the bladder materials to capture its nonlinear elasticity. To develop the nonlinear quasi-static model, several assumptions were made as follows:

Table 2. Energy loss rate of cyclic moment loading.

Test pressures of BE-PAM (kPa)	100	125	150	175	200		Average
Energy loss rate of BE-PAM	28.15%	23.50%	25.26%	28.58%	22.33%		25.57%
Test pressures of BC-PAM (kPa)	40	60	80	100	120	140	Average
Energy loss rate of BC-PAM	25.73%	16.05%	14.39%	18.04%	14.17%	16.06%	20.89% (15.74% after excluding the data at 40 kPa)
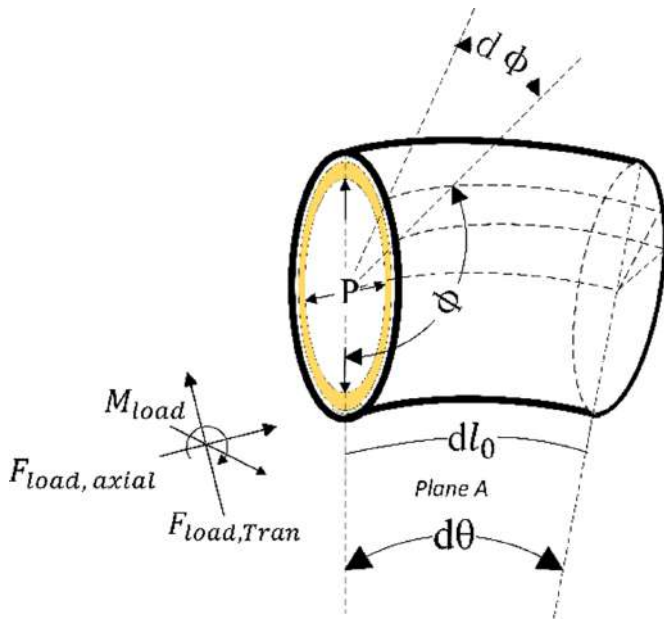
Figure 5. The actuator differential element or unit body with initial length of dl_0.

(a) There is no elastic deformation in the braided sleeve, which means the thread is inextensible and its length is constant.
(b) The friction between the braided sleeve and the bladder is neglected.
(c) The bladder material is incompressible [16].
(d) The cross section of the actuator maintains a circular cross-section before and after actuation.
(e) The length of the elastic frame is constant, but it is flexible without buckling.

3.1. Energy model

A nonlinear energy model was developed for the actuator unit-body with initial length dl_0, based on the principle of virtual work, as shown in figures 2(a) and 5. The Mooney–Rivlin hyperelastic model was used for the elasticity of the bladder.

The following equations can be derived from the work-energy theorem:

$$dW_{in} + dW_{out} = dU \qquad (9)$$

$$dW_{in} = p \, dV_{inner} \qquad (10)$$

$$dW_{out} = -F_{load} ds - M_{load} d\theta \qquad (11)$$

$$dU = d\left(U_{bl} + U_f + U_{br}\right) \qquad (12)$$

where p is the relative working pressure of the actuator, V_{inner} is the inner volume of the bladder, F_{load} and M_{load} are respectively the resulting loaded Force and moment of the element at the frame, ds and $d\theta$ are respectively the linear displacement and rotation angle of the element end, U_{bl} is the elastic energy storage of the bladder, U_f is the elastic energy storage of the elastic frame, and U_{br} is the elastic energy storage of the elastic frame. Due to the inextensible braid material, $dU_{br} = 0$.

As a result of the constraint of the frame, the actuator mainly deforms in plane A, and the out of plane moments and forces were not considered in this model, as shown in figure 5. Meanwhile, F_{load} can be decomposed into axial force $F_{load, axial}$ and transverse shear force $F_{load, tran}$. Due to the inextensible flexible frame and the negligible transverse shear deformation compared with the bending deformation, for the actuator unit-body, when dl_0 is at a minimum, the effect of $F_{load,axial}$ and $F_{load, tran}$ can be neglected compared with that of M_{load}. Hence, only the in-plane bending moment load M_{load} is involved in this model. Nevertheless, for the entire actuator the contribution of force loads can still be calculated by converting them into distributed bending moments.

From the principle of virtual work, the equation can be derived as below:

$$M_{air} = \frac{dW_{in}}{d\theta} = \pi P \left[\left(2R + 3kR^2\right) \frac{dR}{dk'} + R^3 \right] \qquad (13)$$

$$M_E = \frac{dU}{d\theta} = M_f + M_{bl} \qquad (14)$$

$$M_{load} = \frac{dW_{in}}{d\theta} - \frac{d\left(U_{bl} + U_f\right)}{d\theta} = M_{air} - M_E. \qquad (15)$$

Observe that actuation moment of the bending PAM is composed of two terms. M_{air} is the actuation moment due to applied pressure and braid kinematics. M_E is the antagonistic moment considering the elastic energy storage of the bladder and frame. As the axial strain of the elastic frame of fiber-reinforced epoxy is negligible compared to its bending deformation, and the frame is comparatively inextensible comparing with the bladder tube and the braid sleeve, the moment generated by the elastic frame, M_f could be written as follows.
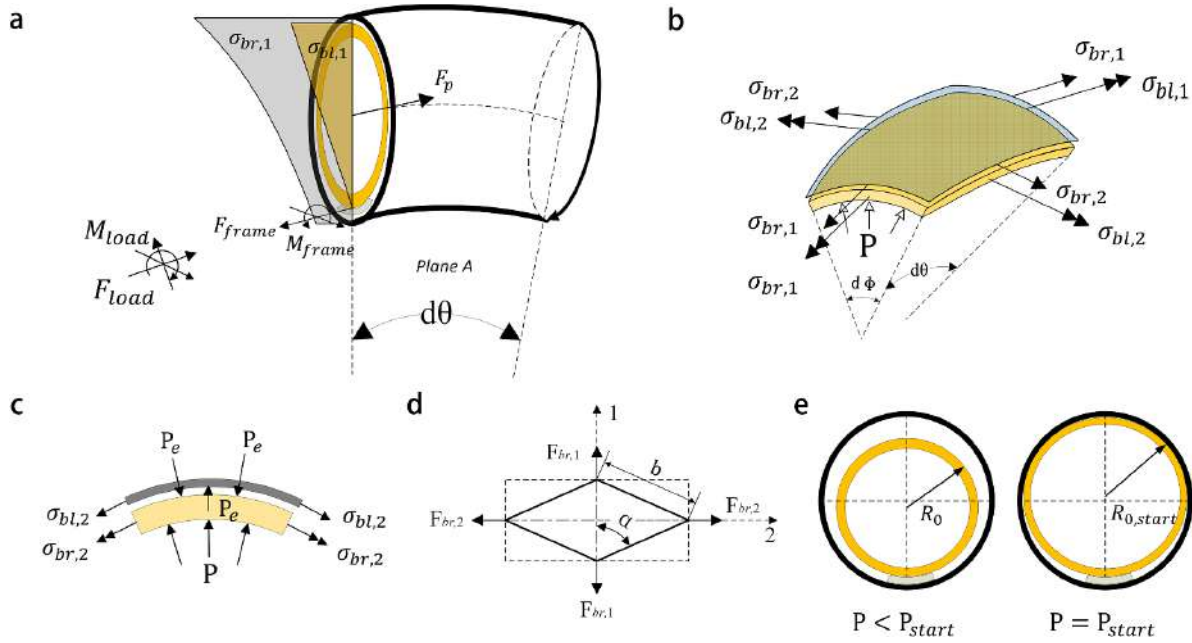
Figure 6. Force balance analysis: (a) force diagram of the actuator unit-body in the axial direction at the cross-section, (b) the free-body diagram of the differential element. (c) hoop stresses and interfacial forces of the free-body differential element. (d) The diamond structure unit cell of the braided sleeve; (e) The actuator cross section in states of $P < P_{\text{start}}$ and $P = P_{\text{start}}$.

$$M_{\text{f}} = \frac{\mathrm{d}U_{\text{f}}}{\mathrm{d}\theta} = E_{\text{f}}I_{\text{f}}k' \tag{16}$$

where the E_{f} is the elastic modulus of the frame and the I_{f} is rotational inertia of the frame.

Here, it is assumed that the axial strain of the bladder are consistent with those of the braid. Also, $\lambda_{\text{bl},1}$, $\lambda_{\text{bl},2}$, and $\lambda_{\text{bl},3}$ are the stretch ratios of the bladder along the axial, circular, and radial directions, respectively. With the Mooney–Rivlin hyperelastic material model and the incompressible property, the following equations can be derived.

$$\lambda_{\text{bl},3} = \frac{\mathrm{t}}{t_0} = \frac{1}{\lambda_{\text{bl},1}\lambda_{\text{bl},2}}, \lambda_{\text{bl},1} = \lambda_1, \lambda_{\text{bl},2} = \frac{R(k')}{R_0} \tag{17}$$

$$W_{bl} = \sum_{i=0,j=0}^{i=1,j=1} C_{ij}\left(\overline{I_1} - 3\right)^i \left(\overline{I_2} - 1\right)^j. \tag{18}$$

With the principle of virtual work, the moment related to the bladder deformation M_{bl} can be derived as follows.

$$M_{\text{bl}} = \frac{\mathrm{d}U_{\text{bl}}}{\mathrm{d}k'}\frac{\mathrm{d}k'}{\mathrm{d}\theta} = (1 + k'R)\left(\int_0^{A_{\text{bl}}} \frac{\mathrm{d}W_{\text{bl}}}{\mathrm{d}k'}\mathrm{d}A\right). \tag{19}$$

By substituting equations (16) and (19) into equation (11):

$$M_{\text{E}} = M_{\text{f}} + M_{\text{bl}} = (1 + k'R)\left(\int_0^{A_{\text{bl}}} \frac{\mathrm{d}W_{\text{bl}}}{\mathrm{d}k'}\mathrm{d}A\right) + E_{\text{f}}I_{\text{f}}k'. \tag{20}$$

The output moment M_{load} can be derived by substituting equations (10) and (20) into equation (12) to obtain:

$$\begin{aligned} M_{\text{load}} = {} & \pi P\left[\left(2R + 3k'R^2\right)\frac{\mathrm{d}R}{\mathrm{d}k'} + R^3\right] \\ & - \left[(1 + k'R)\left(\int_0^{A_{\text{bl}}} \frac{\mathrm{d}W_{\text{bl}}}{\mathrm{d}k'}\mathrm{d}A\right) + E_{\text{f}}I_{\text{f}}k'\right]. \end{aligned} \tag{21}$$

3.2. Force balance model

In this alternative method of derivation, the force balance model for the actuator element was developed using the force analysis of the free bodies shown in figure 6. The Mooney–Rivlin hyperelastic model was also applied to the elasticity of the bladder to describe the nonlinear behavior of the actuator.

Figure 6(a) shows the force balance analysis of the actuator unit-body in the axial direction. The resulting loading force F_{load} and loading moment M_{load} are separately composed of four parts corresponding to the braid, bladder, air pressure and frame as equations (22) and (23), respectively, which are named as F_{br} and M_{br}, F_{bl} and M_{bl}, F_{p} and M_{p}, and F_{br} and M_{br} and can be written as equations (24)–(27).

$$F_{\text{load}} = F_{\text{p}} - F_{\text{frame}} - F_{\text{bl}} - F_{\text{br}} \tag{22}$$

$$M_{\text{load}} = F_{\text{p}}R - M_{\text{frame}} - M_{\text{bl}} - M_{\text{br}} \tag{23}$$

$$F_{\text{br}} = \int_0^{A_{\text{br}}} \sigma_{\text{br},1}\mathrm{d}A, M_{\text{br}} = \int_0^{A_{\text{br}}} \sigma_{\text{br},1}h\mathrm{d}A \tag{24}$$

$$F_{\text{bl}} = \int_0^A \sigma_{\text{bl},1} \mathrm{d}A, M_{\text{bl}} = \int_0^{A_{\text{bl}}} \sigma_{\text{bl},1} h \mathrm{d}A \quad (25)$$

$$F_{\text{p}} = \pi(R-t)^2 P, M_{\text{p}} = \pi(R-t)^2 PR \quad (26)$$

$$M_{\text{frame}} = E_f I_f k' \quad (27)$$

where $\sigma_{\text{br},1}$ is the nominal axial stress of the braid and $\sigma_{\text{bl},1}$ is the axial stress of the bladder.

As mentioned in the energy model, due to the comparatively inextensible frame, M_{load} was only considered for the actuator element. The loading moment M_{load} can be written as follows.

$$M_{\text{load}} = \pi(R-t)^2 PR - E_f I_f k' - \int_0^{A_{\text{bl}}} \sigma_{\text{bl},1} h \mathrm{d}A - \int_0^{A_{\text{br}}} \sigma_{\text{br},1} h \mathrm{d}A. \quad (28)$$

According to the equation (28), in order to obtain the solution of M_{load}, $\sigma_{\text{bl},1}$ and $\sigma_{\text{br},1}$ first need to be solved. To solve the distribution of $\sigma_{\text{bl},1}$ and $\sigma_{\text{br},1}$, a force balance analysis was conducted with the microelement free-body in figure 6(b).

It is assumed that the actuator radius R is far less than the bending radius, i.e. $R_{\text{bend}} = 1/k$, and the elastic tube applies uniform pressure on the braided sleeve. From figures 6(b) and (c), the force balance equation of the bladder microelement can be expressed as

$$-\Delta P \mathrm{d}\theta R(1 + \varepsilon_{\text{bl},1}) \mathrm{d}\varphi$$
$$= \sigma_{\text{bl},2} t(1 + \varepsilon_{\text{bl},1}) \mathrm{d}\varphi \mathrm{d}\theta + \sigma_{\text{bl},1} t \mathrm{d}\theta \frac{R}{R_{\text{bend}}} \mathrm{d}\varphi. \quad (29)$$

Here, $\sigma_{\text{bl},2}$ is the hoop stress of the bladder, and $\Delta P = P_e - P$, where P_e is the interfacial pressure that the bladder applies on the braid sleeve.

As the actuator radius R is far less than the bending radius R_{bend}, the second term on the right hand side can be ignored. Equation (29) can be simplified as below.

$$\sigma_{\text{bl},2} = \frac{-\Delta PR}{t} = \frac{-(P_e - P)R}{t}. \quad (30)$$

With the same approach, the nominal axial stress of the braid $\sigma_{\text{br},1}$ can be formulated as follows:

$$\sigma_{\text{br},2} = \frac{P_e \mathrm{R}}{t_{\text{br}}}. \quad (31)$$

Here, t_{br} is the nominal thickness of the braid sleeve, and $\sigma_{\text{br},2}$ is the nominal circular stress of the braid sleeve.

With the Mooney–Rivlin hyperelastic material model, the following equations are obtained.

$$\sigma_{\text{bl},1} - \sigma_{\text{bl},2} = 2C_1 \left(\lambda_{\text{bl},1}{}^2 - \lambda_{\text{bl},2}{}^2\right) - 2C_2 \left(\frac{1}{\lambda_{\text{bl},1}{}^2} - \frac{1}{\lambda_{\text{bl},2}{}^2}\right) \quad (32)$$

$$\sigma_{\text{bl},2} - \sigma_{\text{bl},3} = 2C_1 \left(\lambda_{\text{bl},2}{}^2 - \lambda_{\text{bl},3}{}^2\right) - 2C_2 \left(\frac{1}{\lambda_{\text{bl},2}{}^2} - \frac{1}{\lambda_{\text{bl},3}{}^2}\right) \quad (33)$$

where $\sigma_{\text{bl},3}$ is the radial stress, and $\lambda_{\text{bl},1}$, $\lambda_{\text{bl},2}$, $\lambda_{\text{bl},3}$ are the stretch ratios of the bladder along the axial, circular, and radial directions, respectively. It is assumed that the axial strain of the bladder is the same as that of the braid. Considering the incompressibility and deformation of the bladder, the stretch ratio equations can be derived as follows.

$$\lambda_{\text{bl},1} = \lambda_1 = 1 + \varepsilon_{\text{bl},1} = 1 + k'h = 1 + k'R(1 - \cos\phi) \quad (34)$$

$$\eta = \frac{R_0}{R} = \frac{1}{2\pi}\int_0^{2\pi} \frac{1}{(1 + \varepsilon_{\text{bl},2})} \mathrm{d}\theta = \frac{1}{2\pi}\int_0^{2\pi} \frac{1}{\lambda_{\text{bl},2}} \mathrm{d}\theta \quad (35)$$

$$\lambda_{\text{bl},3} = \frac{\text{t}}{t_0} = \frac{1}{\lambda_1 \lambda_2}. \quad (36)$$

Previous models regard the bladder as a thin walled tube with the assumption that the bladder wall section only carries stresses in the axial and circular directions. However, in reality, $\sigma_{\text{bl},3} = -\text{P}$ at the inner wall of the tube, and $\sigma_{\text{bl},3} = -P_{\text{eff}}$ at the outer wall [18]. When $\lambda_{\text{bl},1} = \lambda_{\text{bl},2} = \lambda_{\text{bl},3} = 1$, the stresses $\sigma_{\text{bl},1} = \sigma_{\text{bl},2} = \sigma_{\text{bl},3} = -P$, which are demonstrated in models involving the effect of the bladder thickness [16]. Therefore, the radial stress $\sigma_{\text{bl},3}$ is assumed to be $-P$ in this study in order to consider the effect of the thickness and simplify the modeling.

$$\sigma_{\text{bl},3} = -P. \quad (37)$$

With equations (31)–(37), $\sigma_{\text{bl},1}$ and $\sigma_{\text{bl},2}$ could be solved in theory, but the solution procedure and results would be too complex for practical applications, so that an approximate method was employed. Therefore, an assumed solution of the circular stretch ratio $\lambda_{\text{bl},2}$ was used with some compromises in the stress and strain conditions, as shown below.

$$\lambda_{\text{bl},2} = \frac{R}{R_0}. \quad (38)$$

Equation (38) was chosen to satisfy equation (35); however, this also brought conflict to equation (33). To resolve the conflict, the average axial stretch ratio $\overline{\lambda_1}$ and the average thickness $\bar{t}$ were introduced.

$$\overline{\lambda_{\text{bl},1}} = \frac{1}{2\pi}\int_0^{2\pi} \lambda_1 \mathrm{d}\theta = 1 + k'R \quad (39)$$

$$\bar{t} = \frac{t_0}{\overline{\lambda_{\text{bl},1}}\lambda_{\text{bl},2}}. \quad (40)$$

Replacing the $\lambda_{\text{bl},1}$ in equation (36) with $\overline{\lambda_{\text{bl},1}}$, equations (32) and (33) can be rewritten as follows.

$$\sigma_{\text{bl},1} = 2C_1 \left(\lambda_{\text{bl},1}^{\,2} - \frac{1}{\overline{\lambda_{\text{bl},1}}^2 \lambda_{\text{bl},2}^2} \right)$$
$$- 2C_2 \left(\frac{1}{\lambda_{\text{bl},1}^{\,2}} - \overline{\lambda_{\text{bl},1}}^2 \lambda_{\text{bl},2}^2 \right) - P \qquad (41)$$

$$\sigma_{\text{bl},2} = 2C_1 \left(\lambda_{\text{bl},2}^{\,2} - \frac{1}{\overline{\lambda_{\text{bl},1}}^2 \lambda_{\text{bl},2}^2} \right)$$
$$- 2C_2 \left(\frac{1}{\lambda_{\text{bl},2}^{\,2}} - \overline{\lambda_{\text{bl},1}}^2 \lambda_{\text{bl},2}^2 \right) - P. \qquad (42)$$

By substituting equations (36), (38) and (39) into equations (41) and (42), the axial stress and hoop stress of the bladder can be derived, as shown below.

For the actuator with the original radius of R_0 and original braid angle of α_0, $\lambda_2 = \eta = R/R_0$ is only related to the bending curvature k', the axial stress $\sigma_{\text{bl},1}$ is determined by bending curvature k' and cylindrical coordinate Φ at cross section, and the hoop stress $\sigma_{\text{bl},2}$ is only determined by the bending curvature k'.

$$\sigma_{\text{bl},1} = 2C_1 \left(\left(1 + k'R\left(1 - \cos\phi\right)\right)^2 - \frac{1}{\left(1 + k'R\right)^2 \left(\frac{R}{R_0}\right)^2} \right)$$
$$- 2C_2 \left(\frac{1}{\left(1 + k'R\left(1 - \cos\phi\right)\right)^2} - \left(1 + k'R\right)^2 \left(\frac{R}{R_0}\right)^2 \right)$$
$$- P \qquad (43)$$

$$\sigma_{\text{bl},2} = 2C_1 \left(\left(\frac{R}{R_0}\right)^2 - \frac{1}{\left(1 + k'R\right)^2 \left(\frac{R}{R_0}\right)^2} \right)$$
$$- 2C_2 \left(\frac{1}{\left(\frac{R}{R_0}\right)^2} - \left(1 + k'R\right)^2 \left(\frac{R}{R_0}\right)^2 \right) - P. \qquad (44)$$

P_e can be obtained from equation (30) by substituting equation (44) and replacing t with the average thickness of the bladder, $\bar{t}$.

$$P_e = \frac{P\left(R - \bar{t}\right) - \sigma_{\text{bl},2}\bar{t}}{R}. \qquad (45)$$

From figure 6(d), the axial force F_1 and the circular force F_2 of the diamond unit of the braid sleeve are related as shown below.

$$\frac{F_1}{F_2} = \operatorname{atan}\alpha = \frac{\cos\alpha}{\sin\alpha} = \frac{\sin\alpha\,\sigma_{\text{br},1}}{\cos\alpha\,\sigma_{\text{br},2}}. \qquad (46)$$

As the axial stretch ratio $\lambda_1 = \sin\alpha/\sin\alpha_0$ and the circular stretch ratio $\lambda_2 = \sin\alpha/\sin\alpha_0$, the constitutive equations of the braid sleeve can be derived from equation (46) as equation (47).

$$\frac{\sigma_{\text{br},1}}{\sigma_{\text{br},2}} = \tan^2\alpha = \left(\frac{\lambda_1 \cos\alpha_0}{\lambda_2 \sin\alpha_0} \right)^2. \qquad (47)$$

$\sigma_{\text{br},1}$ is the nominal axial stress of the braid sleeve. According to the equations (31), (45) and (47), $\sigma_{\text{br},1}$ can be expressed as equation (48).

$$\sigma_{\text{br},1} == \left(\frac{\lambda_1 \cos\alpha_0}{\lambda_2 \sin\alpha_0} \right)^2 \frac{P\left(R - \bar{t}\right) - \sigma_{\text{bl},2}\bar{t}}{t_{\text{br}}}. \qquad (48)$$

Finally, substitute equations (43) and (48) into equation (28), the formulation of M_{load} was derived as follows.

$$M_{\text{load}} = F_p R - M_{\text{frame}} - M_{\text{bl}} - M_{\text{br}}$$
$$= \pi R^3 P - E_f I_f k' - \int_0^{2\pi} \left(2C_1\left(1 + k'R\left(1 - \cos\phi\right)\right)^2 \right.$$
$$\left. - 2C_2 \frac{1}{\left(1 + k'R\left(1 - \cos\phi\right)\right)^2} \right) \left[R\left(1 - \cos\theta\right)\right]\bar{t}R\,\mathrm{d}\theta$$
$$- 2\pi R^2 \bar{t} \left(2C_1 \frac{1}{\left(1 + k'R\right)^2 \left(\frac{R}{R_0}\right)^2} - 2C_2\left(1 + k'R\right)^2 \left(\frac{R}{R_0}\right)^2 \right) \cdots$$
$$\cdots - \left[P\left(R - \bar{t}\right) - \sigma_{\text{bl},2}\bar{t} \right] R^2 \cos^2\alpha_0$$
$$\int_0^{2\pi} \frac{\left[1 + k'R\left(1 - \cos\theta\right)\right]^2}{1 - \cos^2\alpha_0\left[1 + k'R\left(1 - \cos\theta\right)\right]^2} \left(1 - \cos\theta\right)\mathrm{d}\theta. \qquad (49)$$

3.3. Corrections for working pressure and prestrain

The phenomenon of the pressure deadband has been studied extensively in PAM research [12, 28–31]. From figures 4(c)–(f), it is shown that there is little or no block moment or free-bending motion generated until the threshold of driving pressure, P_{start}, has been reached. This pressure deadband phenomenon [31] is mainly due to the gap between the elastic tube and the braid sleeve at the resting state. An initial pressure is required for the bladder to be inflated and to contact the surrounding braid in order to output bending moment or motion, as shown in figure 6(e). To include this effect of the working pressure deadband in the model, the working pressure P is reduced as follows:

$$P_{\text{active}} = P - P_{\text{start}} \qquad (50)$$

where P is the actual working pressure, P_{active} is active working pressure, and P_{start} is the threshold pressure at which the actuator starts to work.

Moreover, due to the prestrain of the bladder at P_{start}, the outer radius and thickness of the bladder change, which means that the original parameters of the bladder need to be corrected to adapt to the modeling. It was assumed that the length of the bladder remains invariable before the working pressure P

reaches the starting threshold pressure P_{start}. The corrections can therefore be made as shown below.

$$\pi \left[R_{0,\,\text{start}}{}^2 - (R_{0,\,\text{start}} - t_{0,\,\text{start}})^2 \right] = \pi \left[R_0{}^2 - (R_0 - t_0)^2 \right]$$
(51)

$$t_{0,\,\text{start}} = R_{0,\,\text{start}} - \sqrt{R_{0,\,\text{start}}{}^2 - 2R_0 t_0 + t_0{}^2}.$$
(52)

Here, $R_{0,\text{start}}$ and $t_{0,\text{start}}$ are the actuator radius and thickness of bladder, respectively, at P_{start}.

3.4. Experimental validation of analysis

Simulations of the two nonlinear quasi-static models were conducted and compared with the experimental results of the cycling moment load test of BE-PAM and BC-PAM. The input geometry parameters were determined from the PAM geometry measurements, as listed in table 1. The elastic modulus of the elastic sheet frame was defined by a uniaxial tensile test on the Zwick-010 Electro-mechanical Universal Testing Machine, as shown in table 1. The simulations were calculated with set of pressures corresponding to the cyclic loading tests.

As the Mooney–Rivlin coefficients are challenging to determine experimentally, the material parameters were identified via an iterative parameter identification procedure based on the experimental data. The estimated values of $C_1 = 114$ kPa, $C_1 = 300$ kPa were obtained from a tension test of the bladder tube on the Zwick-050 Testing Machine and utilized as the starting value for the iteration process. Moreover, due to the significant influence on the behavior of the actuator and the unavoidable measuring errors, the initial braid angle α_0 was also allowed to float within the range of $\pm 10\%$ to better match with the experiment results.

The modeling results are shown in figure 7 and table 3. Figures 7(a) and (b) show the modeling results of BE-PAM with energy model and force balance model. Both models meet well with the experimental results besides the curves around the free-bending state at 175 kPa and 200 kPa. That was mainly caused by the increasing bending angle and the descending output moment as mentioned in section 2.2, which also appears in the loading curve of BC-PAM at 140 kPa and led to the larger deviation of free-bending curvature between the model and experiment (figures 7(d) and (h)).

Figures 7(e) and (f) show the modeling results of BC-PAM with the two models. Both models also meet well with the experimental results. However the estimated values of block moments is a bit lower than the experimental results (figure 7(g)), which could be the result of the elastic elongation of the fibers in the braid tube, except for the fitting error of models. In the assumptions, the braid fiber is assumed as inextensible, however due to lower braid angle, the braid fiber of BC-PAM bears much larger tension stress, under which the braid fiber extends elastically and the diameter of PAM also becomes larger than models, which could also explain the lower deviation between the estimated and tested block moments of BE-PAM (figure 7(c)). As a result of higher

braid angle, tension stress in the braid fiber of BE-PAM is much lower, so the effect of elastic expansion is less than BC-PAM.

The normalized root mean squared errors (NRMSEs) of BE-PAM and BC-PAM for the energy model about the loading cycles are approximately 3.30% and 5.41%, respectively, that for the force balance model are approximately 3.32% and 5.48% (figures 7(a) and (b) and table 3). The NRMSEs of cyclic loading, block moment and Free Bending Curvature were calculated with equations (53), (54) and (55). $\text{RMES}_{\text{Cylic},i}$, $M_{\text{Max},i}$ and $K_{\text{Max},i}$ are the root mean squared error (RSME), maximum moment and maximum bending curvature of a cyclic loading test under a pressure of P_i. RMES_{BM} and RMES_{FBC} are the RSMEs of block moment and free bending curvature. BM_{Max} and FBC_{Max} are the maximum block moment and free bending curvature of the BE/BC-PAM cyclic loading test.

$$\text{NRMES}_{\text{Cyclic}} = \sqrt{\frac{\sum_{i=1}^{n} \left[\text{RMES}_{\text{Cylic},i} / (M_{\text{Max},i} - 0) \right]^2 K_{\text{Max},i}}{\sum_{i=1}^{n} K_{\text{Max},i}}}$$
(53)

$$\text{NRMES}_{\text{BM}} = \text{RMES}_{\text{BM}} / (\text{BM}_{\text{Max}} - 0)$$
(54)

$$\text{NRMES}_{\text{FBC}} = \text{RMES}_{\text{FBC}} / (\text{FBC}_{\text{Max}} - 0).$$
(55)

As a consequence of the different assumptions, the defined Mooney–Rivlin material coefficients of the energy model are a little different from the force balance model. An equivalent circular cross-section strain was involved to simplify the calculation both in the assumptions of the energy model and the force balance model. However, it is further assumed that the elastic tube applies uniform pressure on the braided sleeve in the force balance model, which generates the distinctions between the two models. In general, the energy model can be derived and expressed in a simpler mathematical form and has a higher accuracy but lacks a comprehensive explanation of the actuating mechanism, while the force balance model further promotes the comprehension of the inner working mechanisms by revealing internal stresses and interaction forces distribution existing in different components.

The two quasi-static nonlinear models were validated and achieved good agreement with load curves for both the BE-PAM and BC-PAM, which demonstrates that the nonlinear model of the bladder material and the variable section profile can accurately predict actuator characteristics.

4. Soft grippers and humanoid hand based on BE-PAMs and BC-PAMs

4.1. Soft three-finger grippers

Two three-finger grippers were developed to investigate the performance of BE-PAMs and BC-PAMs on gripping robot.
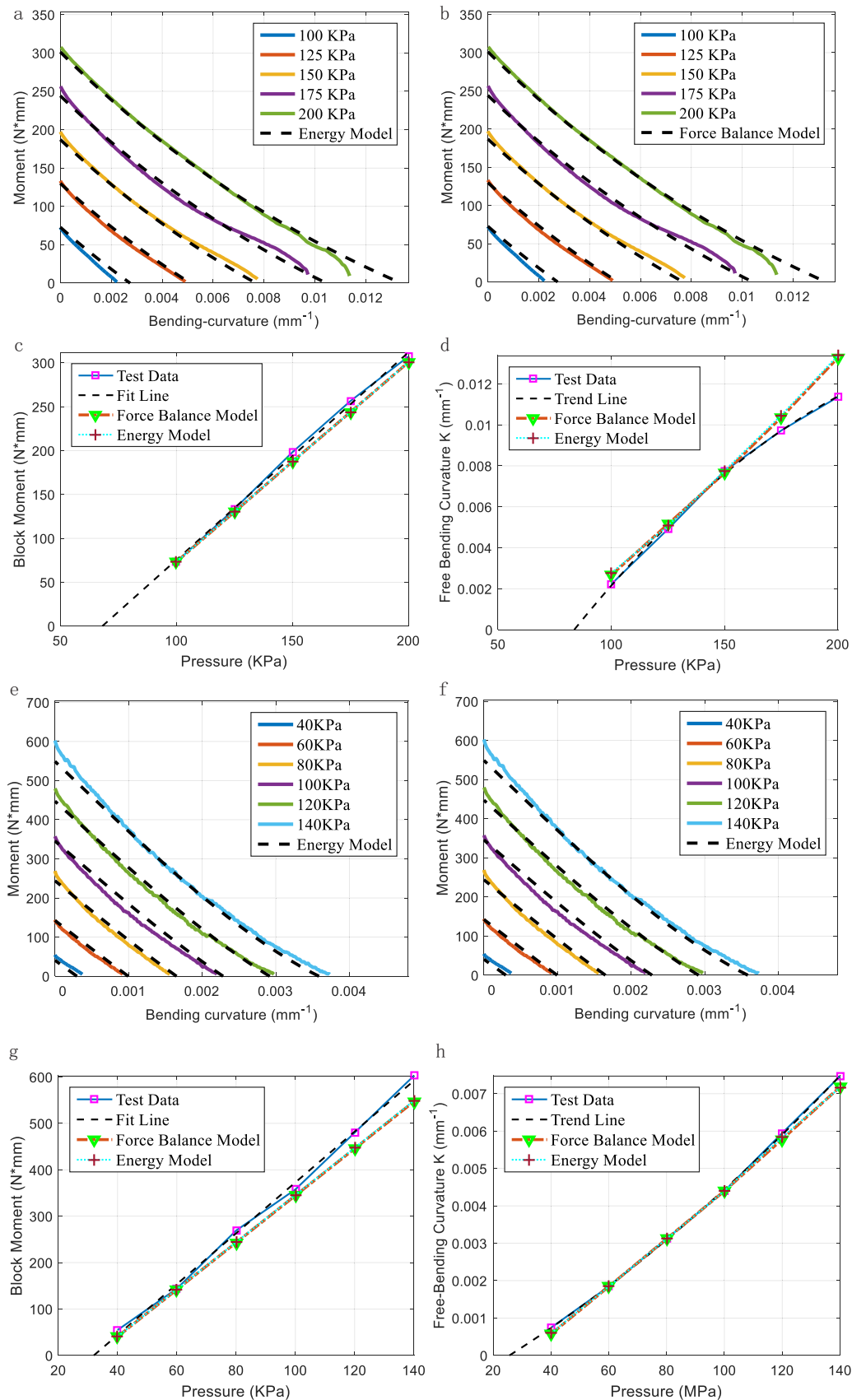
Figure 7. Modeling results using the energy model and the force balance model: analysis of the energy model compared to test data for cyclic loading test of BE-PAM (a) and BC-PAM (e); Analysis of the force balance model compared to test data for cyclic loading test of BE-PAM (b) and BC-PAM (f); Analysis compared to test data for block moments of BE-PAM (c) and BC-PAM (g); Analysis compared to test data for free bending curvature of BE-PAM (d) and BC-PAM (h).

Table 3. Modeling results of Energy model and Force Balance Model.

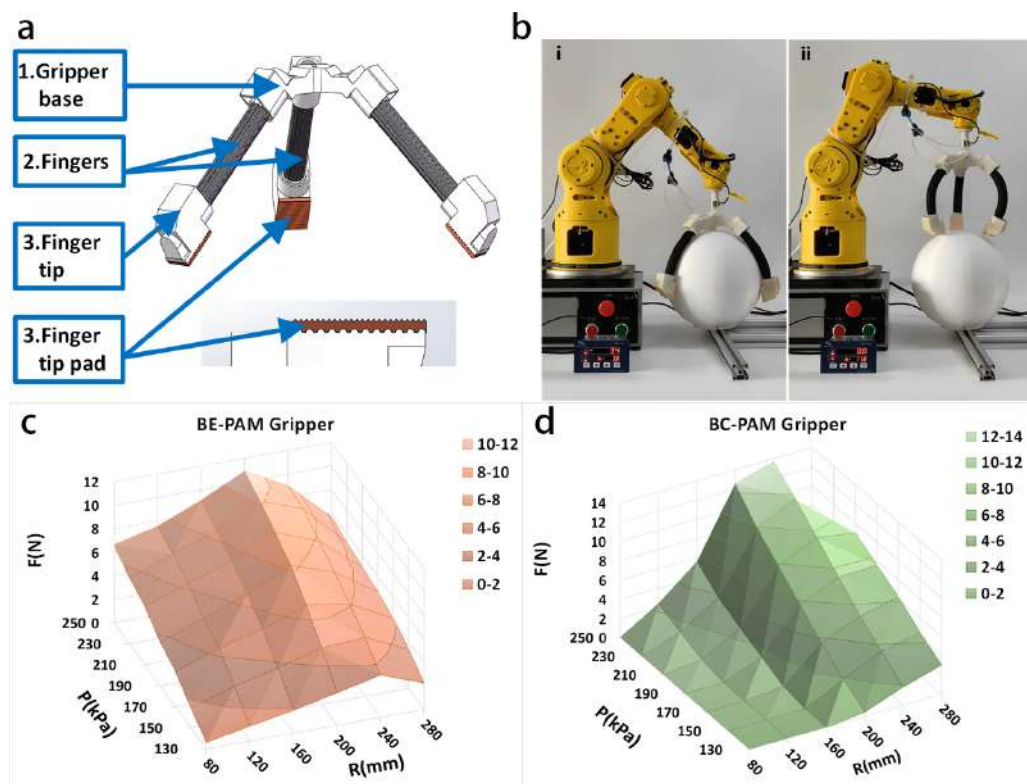|	α_0 /°	$C_{10}\,(C_1)$ kPa^{-1}	$C_{01}\,(C_2)$ kPa^{-1}	The normalized root mean squared error (NRMSE) of loading cycles	The NRMSE of blocked forces	The NRMSE of free bending curvature
Energy model (BE-PAM)	69.7	−318.9	515.5	3.30%	2.63%	8.78%
Force balance model (BE-PAM)	69.7	−133.7	373.3	3.32%	2.64%	8.20%
Energy model (BC-PAM)	36.57	1485.3	−1196.8	5.41%	4.74%	1.92%
Force balance model (BC-PAM)	36.60	1499.9	−1169.9	5.48%	4.94%	2.03%

Figure 8. Soft three-fingered grippers based on BE-PAMs and BC-PAMs. (a) The soft three-fingered gripper, (b) measuring the gripping forces of the three-fingered gripper (BC-PAMs) for a 3D printed sphere with the diameters of 24 cm. (c), (d) Measured gripping forces of two grippers for 3D printed spheres with different diameters from 8.0 cm to 28.0 cm under pressures from 130 kPa to 250 kPa.

The two soft grippers were both composed of three parts, including a hand base, soft fingers and fingertips. Each finger was built with a BE-PAM or BC-PAM. One end of each BE-PAM/BC-PAM, having the ports for inflation and deflation, was fastened to the base, which is shown in figure 8(a).

Two three-finger gripper were built with three BE-PAMs and BC-PAMs with the active length of 13 cm separately. Tip pads made of thermoplastic polyurethane with the Shore hardness of 85 A were attached on the tip to keep the gripping force among measurement range. These pads were also designed with triangular grooves with the height of 0.8 mm, the bottom edge of 1 mm and periodic spacing of 1.5 mm.

The gripping force tests were conducted with the spheres with different diameters from 8 cm to 28 cm at the pressure from 130 kPa to 250 kPa, shown in figure 8(b). These spheres were 3D printed with same material of poly lactic acid, layer height of 0.2 mm and other printing parameters to control the contact conditions such as hardness and texture. In the test, the gripper was fastened on the end of a commercial six-axis manipulator arm (V6PLUS Robotic Arm from RobotAnno (Shen Zhen) Co., Ltd) which owns the positional accuracy of ±0.5 mm. During test, the arm first moved close to the 3D printed sphere, and the gripper was inflated and grasped the ball, then the robot arm pull the gripper away vertically from the sphere with the speed of 3 cm s^{-1}, during
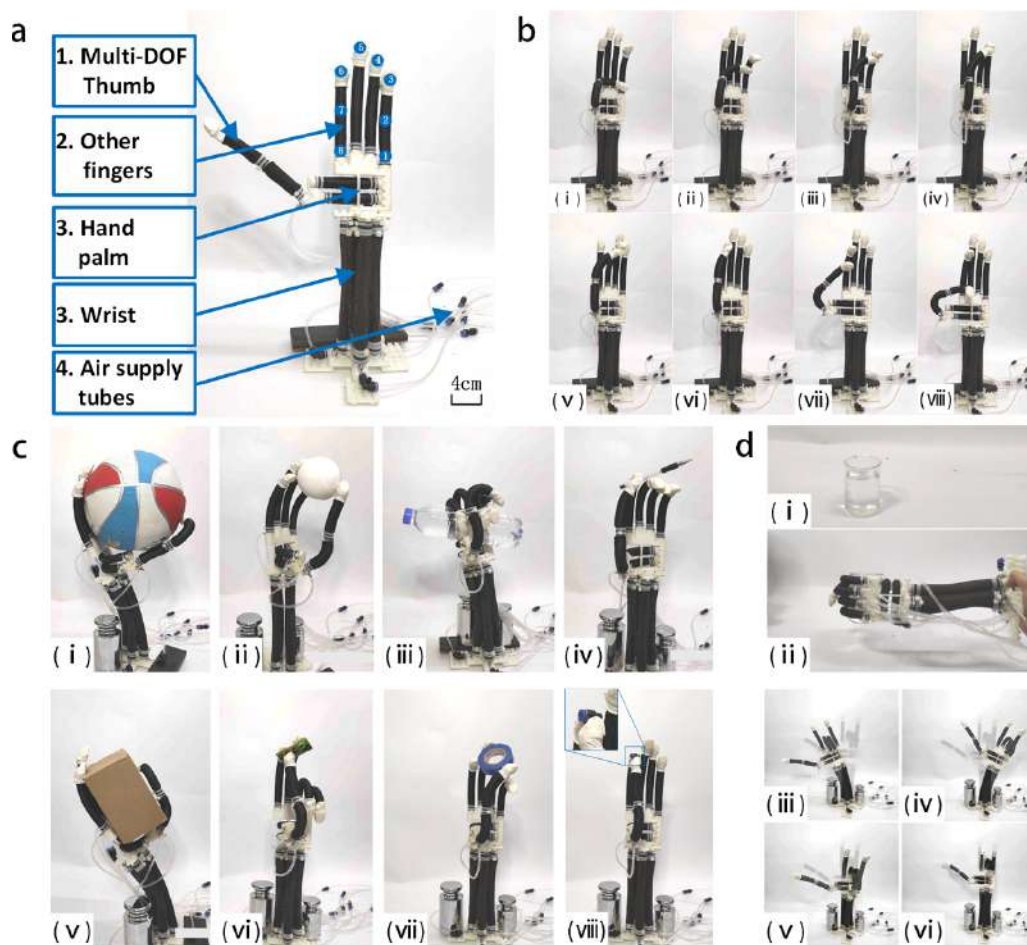
Figure 9. A soft humanoid hand. (a) Components of the humanoid hand. (b) Gestures of dexterous hand (c) gripping objects of different sizes, shapes and stiffness with the soft humanoid hand, (i) a basketball (20.4 cm), (ii) a 3D printed sphere (4 cm), (iii) a bottle full of water (550 g), (iv) a pen, (v) a corrugated paper box, (vi) a circuit board, (vii) a roll of tape, and (viii) a pneumatic quick connector (8 mm). (d)The wrist base on BC-PAMs, (i and ii) holding a bottle of water (335 g) horizontally, (iii–vi) multi-direction bending motion.

which the maximum pulling force were recorded as gripping force.

It was found that the grasping force is almost linear to the applied air pressure for both BE-PAM Gripper and BC-PAM Gripper. The contacting force between the finger and the object increases with the diameter, while the angle of the contacting surface to the gravity vertical decreases. As a result, at higher pressures, the maximum grasping force of the BE-PAM Gripper were obtained when grasping the spheres of 20 cm at 250 kPa instead of the maximum diameter. Though the BC-PAM Gripper failed at 230 kPa when grasping the sphere of 28 cm due to the buckling and fracture of reinforced frame [9], the gripping force data at 210 kPa still indicated that as the diameter of the sphere increases the gripping force would finally decrease, which means the grasping force not only relates to the contacting forces but also to the contacting orientations. Besides, the BE-PAM Gripper showed more accommodative grasping performance for objects with various sizes, which is brought by the larger deformation range and lower variation rate of interaction force to object sizes. Whereas, the BC-PAM Gripper could generate much more gripping force when grasping objects with larger sizes. In a word, compared with the

BC-PAM Gripper, the BE-PAM Gripper showed the larger work space and more excellent compliance which is much useful for grasping smaller object, but BC-PAM Gripper could bear higher loads and provide more stable gripping for larger objects.

4.2. Humanoid hand with multi-direction bending wrist

Based on the characterization tests and the performance of grippers, a soft humanoid hand with multi-direction bending wrist was designed and built based on BE-PAMs and BC-PAMs to better utilize their different features. The humanoid hand was made of fingers, palm and wrist, as figure 9(a). The fingers and palm were actuated by BE-PAM to realize high Flexibility and adaptability in gripping objects. And the wrist was built with four BC-PAMs to achieve four direction bending motions and enhance the load capability.

The thumb has two freedoms of motion in two directions with the intersection angle of 60°, each part of which can bend over 90° (figures 9(a) and (b)). The thumb is fasten on a reconfigurable palm which enables the thumb roll over 90° around the index finger. So the tip of the thumb has three

freedoms of motion in total, which made it succeed in the Kapandji test, a test requires the thumb tip achieves touching eight points on other four figures to evaluate its flexibility, shown in figures 9(a) and (b). It should be noted that though the thumb achieved to touch the point 8, its tip failed to touch the point due to the too close distance between thumb and index. But this does not affect too much on the dexterity on gripping objects. The dexterous hand is able to adapt to diverse objects with various sizes, shapes, weights and materials, shown in figures 9(b) and (c).

And the wrist can not only support the weight of the hand and object but also can adjust the orientation of the hand to improve its gripping performance, especially for large objects, as figure 9(c)—(i) and (v). The wrist is actuated by four symmetrically distributed BC-PAMs, which enables the wrist to bend over 30° in four different directions via inflating the corresponding actuator as figure 9(d)—(iii–vi). Moreover, the wrist also presents descent load capacity in horizontal state via activating the upper BC-PAM as figure 9(b).

The application in soft gripper and humanoid hand demonstrates that BE-PAM and BC-PAM have great potential in soft robotics, nevertheless appropriate types and parameters of bending PAMs should be chosen carefully in the design to maximally utilize their capability and get the best performance.

5. Conclusions

This study investigates and compares the behaviors and properties of BE-PAMs and BC-PAMs with cyclic moment loading tests, nonlinear energy and force balance models and soft robotics devices.

The new loading and processing methods were proposed to conduct a bending moment cyclic loading test and provide a more precise evaluation of the actuator performance. The overall relationships of actuation moment to the bending curvature and inner pressure were mapped via this method. Besides, the damping behaviors of BE and BC PAMs were also investigated for the first time. In addition, the soft grippers demonstrated in this study show the merits of bending PAMs on robotics: low cost, wide range of motion, simple and reliable design, soft and compliant structure, while the BE-PAM gripper showed more compliance. It can be drawn that the BE-PAM exhibit larger scale deformability and outstanding compliance, while the BC-PAM show higher output capacity and efficiency, which indicates the wide range output performance and designability of bending PAMs and implies their promising prospects on soft robotics and wearable devices such as soft sorting manipulators, bio-robots, assistant exo-suits and force feedback wearable devices. Nevertheless, it should be noted that during the tests, especially in the tests of soft grippers and humanoid hand, some limitation of BE-PAM and BC-PAM also were revealed. BE-PAMs are easily interfered by external forces due to its relative low stiffness. For example, BE-PAMs is liable to be distorted under out-plane loads which may affect gripping stability of grippers built with it. While BC-PAM has

higher stiffness and is less liable to be distorted, its inner frame bears high compressing force and is easy to buckle and fracture under high inner pressure or external loads, which would lead to the failure. Further works on out-plane and buckling behaviors of bending PAMs are needed to explain, predict to improve their performances.

The most significant contribution of this research is proposing two nonlinear quasi-static models based on the principle of virtual work and force balance analysis. The models predicted the nonlinear behavior of the actuators well with the relative error around 5%. Meanwhile the two models further promote the comprehension of the inner working mechanisms by revealing interactions among different components and relationships between the output moment and the actuator parameters. The experimental and modeling efforts also provide a valuable reference for others analyzing and utilizing actuators with similar structures.

However, the hysteresis effect has not been included in the model of this work, which also has much influence on the output performance especially for the dynamic behaviors. And in this work, only in-plane bending moment was considered, while in many cases, the load conditions of actuators are much more complex, including out-plane force/moment/torsion, concentrated/distributed force/moment and non-uniform load distribution. Even though some in-plane loads can be treat as non-uniform distributed bending moments, the behaviors of bending PAMs under out-plane loads still need further studies and modeling works, and in some situations shear and torsional deformation of the bending PAMs would be non-negligible. So in the future, more studies will be conducted with the mechanism and modeling of their hysteresis effect, dynamic behaviors and complex load conditions to build better prediction model for the analysis, design and control of bending PAMs and the mechanisms/robots based on them. Furthermore, it would be also possible that these modeling and analysis works were expanded to these more complicate actuators following the same principles, such as helical, twist and multi-DOF PAMs.

ORCID iDs

Qinghua Guan https://orcid.org/0000-0001-5438-9232
Yanju Liu https://orcid.org/0000-0001-8269-1594
Norman M Wereley https://orcid.org/0000-0002-9932-6988
Jinsong Leng https://orcid.org/0000-0001-5098-9871

References

[1] Andrikopoulos G, Nikolakopoulos G and Manesis S 2011 *19th Mediterranean Conference on Control & Automation (MED)* (https://doi.org/10.1109/MED.2011.5982983)

[2] Mcmahan W, Chitrakaran V, Csencsits M and Dawson D 2006 *Proceedings 2006 IEEE International Conference on Robotics and Automation* 2336–41

[3] Kim S, Laschi C and Trimmer B 2013 *Trends Biotechnol.* **31** 287

[4] Pillsbury T E, Guan Q and Wereley N M 2016 *2016 IEEE International Conference on Advanced Intelligent Mechatronics* 94–99

[5] Al-Ibadi A, Nefti-Meziani S and Davis S 2017 *23rd International Conference on Automation and Computing* 1–6

[6] Guan Q, Sun J, Liu Y and Leng J 2017 *21st International Conference on Composite Materials* (*Xi'an*) 4510 (http://www.iccm-central.org/Proceedings/ICCM21proceedings/papers/4510.pdf)

[7] Hassanin A F, Steve D and Samia N M 2018 *Robotics and Autonomous Systems* **99** 63–74

[8] Al-Fahaam H, Davis S and Nefti-Meziani S 2017 *Robot. Auton. Syst.* **99** 63–74

[9] Guan Q, Sun J, Liu Y, Wereley N M and Leng J 2019 *Soft Robotics* **7** 597–614

[10] Al-Fahaam H, Nefti-Meziani S, Theodoridis T and Davis S 2018 *Soft Robot.* **5** 576–591

[11] Polygerinos P, Wang Z, Overvelde J T B, Galloway K C, Wood R J, Bertoldi K and Walsh C J 2015 *IEEE Trans. Robot.* **31** 778–89

[12] Tsagarakis N and Caldwell D G 2002 *IEEE International Conference on Robotics and Automation, ICRA* 3641–46

[13] Tondu B and Lopez P 2000 *IEEE Control Syst.* **20** 15–38

[14] Chou C P and Hannaford B *IEEE Trans. Robot. Autom.* 1996 **12** 90–102

[15] Ferraresi C, Franco W and Bertetto A M 2007 *Journal of Robotics and Mechatronics* **13** 56–63

[16] Wang G, Wereley N M and Pillsbury T 2015 *J. Intell. Mater. Syst. Struct.* **26** 541–53

[17] Yu Z, Pillsbury T, Wang G and Wereley N M *Smart Mater. Struct.* 2019 **28** 105019

[18] Ball E and Garcia E 2016 *J. Med. Device* **10** MED-14-1004

[19] Antonelli M G, Zobel P B, Durante F and Raparelli T 2017 *J. Intell. Mater. Syst. Struct.* **28** 1045389X1769824

[20] Tondu B 2012 *J. Intell. Mater. Syst. Struct.* **23** 225–53

[21] Zhang Z and Philen M 2012 *J. Intell. Mater. Syst. Struct.* **23** 255–68

[22] Zhang J F, Yang C J, Chen Y, Zhang Y and Dong Y M 2008 *Mechatronics* **18** 448–57

[23] Peele B N, Wallin T J, Zhao H and Shepherd R F 2015 *Bioinsp. Biomim.* **10** 055003

[24] Natividad R, Del Rosario M Jr, Chen P and Yeow C H 2018 *Soft Robot.* **5** 304–17

[25] Polygerinos P, Lyne S, Wang Z, Nicolini L F, Mosadegh B, Whitesides G M and Walsh C J 2015 *IEEE Transactions on Robotics* **31** 778–89

[26] Hong K Y, Hui Y N and Yeow C H 2016 *Soft Robotics* **3** 144–58

[27] Wang Z, Polygerinos P, Overvelde J, Galloway K, Bertoldi K and Walsh C 2016 *IEEE/ASME Trans. Mech.* **22** 717–27

[28] Volder M D, Moers A J M and Reynaerts D 2011 *Sensors Actuators* A **166** 111–16

[29] Chou C P and Hannaford B 1996 *IEEE Transactions on Robotics and Automation* **12** 90–102

[30] Solano B and Rotinat-Libersa C 2010 *J. Intell. Mater. Syst. Struct.* **22** 1479–87

[31] Hocking E G and Wereley N M 2013 *Smart Mater. Struct.* **22** 014016